Structural and Multidisciplinary Optimization (2020) 61:2629–2639
https://doi.org/10.1007/s00158-020-02525-3

RESEARCH PAPER

Numerical investigation of stiffness and buckling response of simple and optimized infill structures

Fengwen Wang[1] · **Ole Sigmund**[1]

Received: 16 September 2019 / Revised: 5 December 2019 / Accepted: 16 December 2019 / Published online: 24 February 2020

Abstract
This study systematically investigates stiffness and buckling response of finite structures consisting of repeated unit cells of a reference truss lattice microstructure and a topology optimized microstructure with enhanced buckling strength. Structural stability is evaluated using linear buckling, nonlinear pre-buckling, and post-buckling analyses, subjected to two benchmark loading cases representing uniaxial compression and shear loading. Numerical results indicate that geometric and material nonlinearities play a surprisingly small role in uniaxial loading, whereas strong effects are seen for the shear loading case for which the microstructure was not optimized.

Keywords Structural stability · Finite periodic structures · Linear buckling analysis · Nonlinear pre-buckling analysis · Post-buckling analysis

1 Introduction

Advances in additive manufacturing facilitate the fabrication of functional materials with unprecedented complexity (Meza et al. 2015; Zheng et al. 2016). This leads to increasing attention on architected materials exhibiting enhanced properties and multi-functionalities and in designing multi-level hierarchical lattice structures. Materials with exotic properties have for decades been systematically designed using topology optimization methods (Bendsøe and Sigmund 2003), covering extreme stiffness (Sigmund 1994, 1995; Guest and Prévost 2006; Huang et al. 2011), prescribed negative Poisson's ratio (Sigmund 1995; Larsen et al. 1997; Andreassen et al. 2014; Vogiatzis et al. 2017), programmable auxetic behaviors (Clausen et al. 2015; Wang 2018), zero and negative thermal expansion coefficients (Sigmund and Torquato 1997; Takezawa and Kobashi 2017), extreme buckling strength (Neves et al. 2002; Thomsen et al. 2018), and acoustic topological insulators (Christiansen et al. 2019). Recently, topology optimization methods have been employed to design structures with enhanced stiffness considering 3D printing infill (Wang et al. 2016; Wu et al. 2017) or mapped first-level hierarchical materials (Groen and Sigmund 2018; Allaire et al. 2019).

In addition to stiffness, buckling failure strength in materials or structures is also a fundamental and challenging issue. Even though structures with 3D printing infills in Wu et al. (2017) or mapped first-level hierarchical materials in Groen and Sigmund (2018) and Allaire et al. (2019) do not outperform their solid counterparts regarding stiffness, they may possess an advantage from the buckling strength perspective (Clausen et al. 2016). Material instabilities may develop with different wavelengths spanning from highly localized modes on the microscale to long-wavelength modes on the macro-scale, and material and geometric nonlinearities further complicate the material instability studies. Previous numerical studies have resorted to simplified models which employ homogenization methods for separating scales (Guedes and Kikuchi 1990) and Bloch–Floquet theory for detecting microscopic and macroscopic instabilities (Geymonat et al. 1993). A general methodology for characterizing material strength due to bifurcation failure was proposed in Triantafyllidis and Schnaidt (1993). Later, this method was used to form analytic expressions for

Responsible Editor: Mehmet Polat Saka

✉ Fengwen Wang
fwan@mek.dtu.dk

Ole Sigmund
Sigmund@mek.dtu.dk

[1] Department of Mechanical Engineering, Technical University of Denmark, Nils Koppels Allé 404, 2800 Kongens Lyngby, Denmark

the failure surfaces of simple honeycomb microstructures (Haghpanah et al. 2014). A wide range of material configurations has been investigated in search for improved buckling strength, including 2D honeycombs (Triantafyllidis and Schraad 1998), lattice structures (Meza et al. 2017), and thin-walled structures (Rammerstorfer et al. 2006). It has been discovered that geometric attributes play an essential role in the material buckling strength. Topology optimization of material strength was first studied in Neves et al. (2002), where only cell-periodic buckling modes were taken into account. Later, this work was extended to cover both local and global modes via the Bloch–Floquet theory (Neves et al. 2002). More recently, materials with enhanced buckling strength (Thomsen et al. 2018) have been systematically designed using topology optimization methods for different macro-level stress situations based on the homogenization theory, linear buckling (LB) analysis, and Bloch–Floquet theory. It was shown that the optimized first-order hierarchical materials outperform their non-hierarchical counterparts at the cost of decreased stiffness.

It is an on-going discussion whether structures optimized under LB analysis will perform well in reality or under more realistic nonlinear modeling assumptions. Also, it is not clear how a microstructure optimized under assumption of infinite periodicity will perform in a finite strain modeled, finite structure. Geometric and material nonlinearities as well as boundary effects may cause stiffening or softening effects depending on loading cases and microscale topologies. These open ends deserve further and more systematic investigations.

In this study, we aim at systematically investigating the performance of finite size structures formed from different periodic microstructures regarding stiffness and stability, based on different buckling strength evaluation criteria. The considered microstructures comprise a simple reference microstructure (RMS) and a topology optimized microstructure (OMS) with enhanced buckling strength from Thomsen et al. (2018). Two benchmark problems are formulated, i.e., uniaxial compression loading and shear loading. Although the OMS was optimized for hydrostatic loading, we consider the uniaxial loading case here in order to comply with on-going experimental verification studies. The buckling strength is evaluated using LB, nonlinear pre-buckling (NPB), and post-buckling (PB) analysis. The performance of structures with different infill periods is systematically investigated and compared. Numerical studies confirm the stability enhancement of the OMS in compression dominated finite structures. However, the linearly predicted indirect buckling enhancement in shear loading (not optimized for) degrades or even vanishes, due to nonlinear effects.

The remainder of the paper is organized as follows: Section 2 presents the benchmark problems, different approaches employed to evaluate structural buckling strength, and the hyperelastic material law describing the base material behavior under finite deformations. Section 3 presents the numerical results for the two benchmark problems. An extended discussion is provided in Section 4 and conclusions are drawn in Section 5.

2 Benchmark problems and computational methodologies for buckling evaluations

In this section, we focus on presenting the benchmark problems considered in this study. Based on this, we present the computational approaches used to evaluate the structural buckling strength.

2.1 Benchmark problems and considered infills

In order to evaluate the performance of the considered material configurations, we consider a square structure infilled by N-by-N unit cells with a constant size of $l = 10$ cm and thickness of $t = 1$ cm. As illustrated in Fig. 1a, the left boundary of the structure is clamped, and the right is subjected to uniform displacements denoted by $[u_0, v_0]$. Under above boundary conditions, a uniaxial compression test can be mimicked by constantly reducing u_0 while keeping $v_0 = 0$. The zero vertical deflections at both ends are used to comply with physical compression tests where friction between loading surfaces and samples or an attached solid loading domain efficiently will work as fixed vertical boundary conditions. A shear loading test can similarly be mimicked by prescribing v_0 with free u_0.

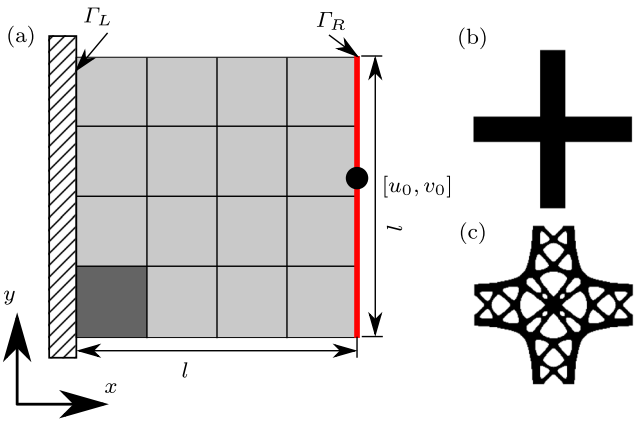

Fig. 1 **a** Schematic illustration of the benchmark problems for the considered structure consisting of N-by-N unit cells with $l = 10$ cm and thickness of $t = 1$ cm. The dark region represents one unit cell. Γ_L and Γ_R represent the left and right boundaries, respectively. **b** RMS. **c** First-order hierarchical OMS that optimizes buckling strength for hydrostatic compression (from Thomsen et al. (2018))

Under above defined boundary conditions, the corresponding effective strain is as follows:

$$\begin{aligned} \varepsilon_{\mathrm{xx}} &= \frac{u_0}{l}, \qquad \text{for uniaxial compression} \\ \varepsilon_{\mathrm{xy}} &= \frac{v_0}{2l}, \qquad \text{for shear loading} \end{aligned} \tag{1}$$

The considered infill microstructures are the RMS in Fig. 1b and the topology OMS with enhanced buckling strength for hydrostatic compression from Thomsen et al. (2018) in Fig. 1c. Hereafter, we refer to them as the RMS and the OMS, unless otherwise stated. The first-order hierarchical configuration OMS is represented by the exact solution and discretization obtained in Thomsen et al. (2018) but thresholded to a pure zero-one design where void elements are removed for simplification of analyses.

2.2 Computational methodologies for buckling strength evaluations

The finite element method is used to determine the critical buckling stress for the proposed benchmark structures. Three approaches are employed and investigated, i.e., LB, NPB, and PB analyses.

The LB analysis here assumes perfect structures, and hence geometric imperfections stemming from the manufacturing process are ignored. Under a small deformation assumption, the static equilibrium of the benchmark problem is governed by the following:

$$\begin{aligned} \boldsymbol{K}_0 \boldsymbol{u}_0 &= \boldsymbol{0}, \\ \boldsymbol{u} &= \boldsymbol{0}, \qquad \text{on } \Gamma_L, \\ \boldsymbol{u} &= [u_0,\ v_0]^T, \qquad \text{on } \Gamma_R. \end{aligned} \tag{2}$$

Here, $\boldsymbol{K}_0$ is the linear stiffness matrix and $\boldsymbol{u}_0$ is the equilibrium displacement vector. Γ_L and Γ_R denote the left and right boundaries, respectively. The total reaction forces on the right boundary are calculated using the following:

$$\boldsymbol{f}^{\mathrm{rect}} = \left[f_x^{\mathrm{rect}},\ f_y^{\mathrm{rect}}\right]^T = \left[\sum_{i\in\Gamma_R} f_{x,i}^{\mathrm{int}},\ \sum_{i\in\Gamma_R} f_{y,i}^{\mathrm{int}}\right]^T. \tag{3}$$

Here, i refers to the nodal number and $f_{x,i}^{\mathrm{int}}$, $f_{y,i}^{\mathrm{int}}$ are the corresponding internal loads in the x- and y-direction, respectively,

Assuming that displacements at the buckling point are small and that stresses are proportional to the prescribed displacements on the boundaries, the stress stiffening effects due to mechanical loading can be evaluated in terms of the displacements determined by linear static analysis. The critical buckling stress is estimated by LB analysis via the following eigenvalue problem,

$$\left[\boldsymbol{K}_0 + \tau \boldsymbol{K}_\sigma\left(\boldsymbol{u}_0\right)\right]\boldsymbol{\phi} = \boldsymbol{0} \tag{4}$$

where $\boldsymbol{K}_\sigma\left(\boldsymbol{u}_0\right)$ is the stress stiffness matrix obtained based on linear elasticity (Wriggers 2008), and $\boldsymbol{\phi}$ is the buckling mode for the eigenvalue τ. The critical buckling stress factor is estimated by the smallest eigenvalue τ_1,

$$\begin{aligned} \sigma_{\mathrm{xx}}^{\mathrm{cri}} &= \tau_1 \bar{\sigma}_{\mathrm{xx}} = \tau_1 \frac{f_x^{\mathrm{rect}}}{lt}, \qquad \text{for uniaxial compression} \\ \sigma_{\mathrm{xy}}^{\mathrm{cri}} &= \tau_1 \bar{\sigma}_{\mathrm{xy}} = \tau_1 \frac{f_y^{\mathrm{rect}}}{lt}, \qquad \text{for shear loading} \end{aligned} \tag{5}$$

where $\bar{\sigma}_{\mathrm{xx}}$ and $\bar{\sigma}_{\mathrm{xy}}$ are the averaged stress in the x-direction and the averaged shear stress, respectively.

Alternatively, one can perform geometric nonlinear analysis on a perfect structure with repeated buckling analysis, to more accurately predict the buckling strength in the deformed state. Here, we use the total Lagrangian approach for the description of geometric nonlinearity. The structural equilibrium is controlled by the following:

$$\boldsymbol{r}\left(\boldsymbol{u}\right) = \boldsymbol{f}^{\mathrm{int}}\left(\boldsymbol{u}\right) = \boldsymbol{0}. \tag{6}$$

Here, $\boldsymbol{u}$ is the nodal displacement vector and $\boldsymbol{r}\left(\boldsymbol{u}\right)$ and $\boldsymbol{f}^{\mathrm{int}}\left(\boldsymbol{u}\right)$ are the corresponding residual and internal load vectors, respectively. The internal nodal force vector is defined by the following:

$$\boldsymbol{f}^{\mathrm{int}}\left(\boldsymbol{u}\right) = \sum_e \boldsymbol{f}_e^{\mathrm{int}}\left(\boldsymbol{u}_e\right) = \sum_e \frac{\partial\left(\int_{v_e} W\left(\boldsymbol{u}_e\right) dv\right)}{\partial \boldsymbol{u}_e}. \tag{7}$$

Here, e represents the element number and $W\left(\boldsymbol{u}_e\right)$ is the stored elastic energy density defined by a hyperelastic material law. The corresponding tangent stiffness matrix is written as follows:

$$\boldsymbol{K}_t\left(\boldsymbol{u}\right) = \sum_e \boldsymbol{K}_{te} = \sum_e \frac{\partial \boldsymbol{f}_e^{\mathrm{int}}}{\partial \boldsymbol{u}_e} = \boldsymbol{K}\left(\boldsymbol{u}\right) + \boldsymbol{K}_\sigma\left(\boldsymbol{u}\right), \tag{8}$$

where $\boldsymbol{K}_{te}$ is the elemental tangent stiffness of element, e, $\boldsymbol{K}\left(\boldsymbol{u}\right)$ is the displacement dependent elastic stiffness matrix, and $\boldsymbol{K}_\sigma\left(\boldsymbol{u}\right)$ is the stress stiffness matrix stemming from the second Piola–Kirchhoff stress.

The static equilibrium, (6), is solved iteratively using the arc-length method in Krenk (2009) via the incremental equation at the nth step stated as follows:

$$\begin{aligned} \boldsymbol{K}_t\left(\boldsymbol{u}^n, \alpha^n\right)\Delta \boldsymbol{u}^n &= \boldsymbol{r}^n, \\ \boldsymbol{u}_i^n &= \boldsymbol{0}, \qquad i \in \Gamma_L, \\ &\text{uniaxial compression:} \\ \boldsymbol{u}_{x,i}^n &= \alpha^n \Delta u_0,\ \boldsymbol{u}_{y,i}^n = 0,\ i \in \Gamma_R, \\ &\text{shear loading:} \\ \boldsymbol{u}_{y,i}^n &= \alpha^n \Delta v_0, \qquad i \in \Gamma_R, \end{aligned} \tag{9}$$

Here, $\Delta \boldsymbol{u}^n$ is the incremental displacement vector and α is the control parameter according to the applied boundary displacements. $\boldsymbol{u}_{x,i}^n$ and $\boldsymbol{u}_{y,i}^n$ are displacements of the node i along the x- and y-direction, respectively, Δu_0 and Δv_0 are the prescribed displacement increments. Detailed

description of the arc-length algorithm can be found in Krenk (2009).

At each equilibrium state, an upcoming buckling point may be predicted based on the current tangent stiffness. Assuming the current configuration is close to the critical point, the stress stiffness part of the tangent stiffness at the critical point is approximated by extrapolating the nonlinear stress stiffness from the current configuration using a factor γ, while the elastic stiffness is assumed to not change with additional loading (Wriggers 2008). Hence, the critical factor can be approximated by an eigenvalue problem as follows:

$$[\boldsymbol{K}(\boldsymbol{u}) + \gamma \boldsymbol{K}_{\sigma}(\boldsymbol{u})]\boldsymbol{\phi} = \boldsymbol{0}. \tag{10}$$

The critical buckling stress is determined by the smallest eigenvalue of (10) and is written as follows:

$$\sigma_{\mathrm{xj}}^{\mathrm{cri}} = \gamma_1 \bar{\sigma}_{\mathrm{xj}} = \gamma_1 \frac{f_j^{\mathrm{rect}}}{lt}, \qquad j \in \{x, y\} \tag{11}$$

where the definition of f_j^{rect} is the same as in (3) for different loading cases. Different from the linear case, the internal force is here calculated based on finite deformations using (7). It is remarked that $\gamma_1 > 1$ indicates that the current deformation is below the buckling point and is stable, and $\gamma_1 < 1$ indicates that the structure is beyond the buckling point. $\gamma_1 = 1$ signifies the stability limit. Hence, the intersection between the critical buckling prediction and the stress–strain curve is the critical buckling stress. This procedure is called NPB analysis in this study.

In PB analysis, the same nonlinear analysis is performed using the arc-length method, however, with the presence of geometric imperfections. Geometric imperfections stemming from the manufacturing procedure stimulate buckling in the nonlinear analysis. The critical buckling stress can be detected by monitoring the tangent stiffness defined by the following:

$$\bar{E}_{\mathrm{xj}} = \frac{\Delta\sigma_{\mathrm{xj}}}{\Delta\varepsilon_{\mathrm{xj}}}, \qquad j \in \{x, y\} \tag{12}$$

The buckling point in the PB analysis is defined by the state where the structure looses considerable stiffness for the first time. Here, we define this state as the load where the stiffness has decreased to 20% of the initial one.

The geometric imperfections here are represented by a set of linear buckling modes with maximum perturbation amplitude, φ. The geometric imperfections are taken into account by modifying each nodal location according to the considered buckling modes scaled by $\varphi / |\max(\boldsymbol{\phi})|$. Nodal positions are equal to the sum of the original positions and perturbations from the buckling modes.

2.3 Hyperelastic material law

We utilize a modified compressible Neo–Hookean material law (Zienkiewicz and Taylor 2005) to describe the material behavior under finite deformations. The corresponding material stored energy density is written as follows:

$$W = \frac{1}{2}\lambda_0 (J-1)^2 + \frac{\mu_0}{2}(I-3) - \mu_0 \ln(J), \tag{13}$$

where $\boldsymbol{F}$ is the deformation gradient and $J = \det(\boldsymbol{F})$; $I = \mathrm{trace}(\boldsymbol{C})$ with $\boldsymbol{C} = \boldsymbol{F}^T\boldsymbol{F}$ being the right Cauchy–Green deformation tensor; λ_0 and μ_0 are the Lamé parameters of the base material.

The benchmark problems are assumed to be under the plane stress assumption, and Young's modulus and Poisson's ratio of the base material are $E_0 = 1$ and $\nu = 0.3$. This corresponds to the values used in Thomsen et al. (2018). When considering finite deformations, it is necessary to modify the constitutive terms to enforce zero stress in the out-of-plane direction, and thus account for the deformation gradient in the out-of-plane direction. The detailed implementation follows Chapter 6.2.4 in Zienkiewicz and Taylor (2005) and is not stated here.

In the PB analysis, the convergence criterion is set to be $\|\boldsymbol{r}\| < 10^{-4}\|\boldsymbol{r}_0\|$ with a maximum of 30 iterations for each displacement increment. Here, $\boldsymbol{r}_0$ is the linear reaction force vector resulting only from the prescribed displacement increment. In the uniaxial compression case, the displacement increment for the OMS is $\Delta u_0 = 0.0280$ cm, and a smaller displacement increment of $\Delta u_0 = 0.0040$ cm is used for the RMS since its buckling strain is much smaller compared to the OMS. In the shear loading case, the displacement increment of $\Delta v_0 = 0.200$ cm is employed. The increment steps are set to be 50 for all the cases. If the arc-length method does not converge within 30 iterations in one displacement increment step, the displacement increment is halved, and the displacement increment step restarts. If the arc-length method converges and displacement increment is smaller than the initial one, the displacement increment is doubled for the next displacement increment.

3 Numerical results

Structures consisting of 2-by-2, 4-by-4, 6-by-6, and 8-by-8 unit cells are considered to account for size effects while keeping the structural size fixed. Each unit cell is discretized by 200 × 200 4-node quadrilateral finite elements as in Thomsen et al. (2018). The volume fraction of the unit cells presented in Fig. 1b, c is 30%, and void

regions are eliminated in the numerical simulations. Both the microstructures are orthotropic and possess the same properties along the two axial directions due to square symmetry. First, we consider the infinitely periodic case. Table 1 presents the effective material properties of the two infinitely periodic materials and the corresponding material buckling strength under uniaxial compression $\left(\sigma_{xx}^{cri}\right)$ and under pure shear loading $\left(\sigma_{xy}^{cri}\right)$. They are estimated by employing the homogenization method and Bloch–Floquet theory to capture both long- and short-wavelength buckling modes as presented in Thomsen et al. (2018).

As seen in Table 1, the OMS exhibits smaller bulk and Young's moduli than the RMS, whereas it possesses much higher shear modulus. The material buckling strength of the OMS is 4.5 times the one of the RMS under uniaxial compression. Figure 2 a and b display the critical material buckling modes under uniaxial compression extrapolated over 4-by-4 unit cells. The critical buckling mode of the RMS is a global shear mode, whereas the one of the OMS is an anti-periodic mode spanning two cells. It is worthwhile mentioning that a cluster of material buckling modes in the OMS display buckling stress very close to the critical one.

Figure 2 c and d present the critical material buckling modes for pure shear loading. The buckling mode in the RMS expands over two periods in the vertical direction, while the one in the OMS is an anti-periodic mode in both the x- and y-directions. The buckling strength enhancement of the OMS degrades to be around 3.3 times that of the RMS.

In the linear finite cell analysis, the effective Young's modulus is measured from the uniaxial compression as $E^H = \sigma_{xx}/\varepsilon_{xx}$, and the effective shear modulus is measured from the shear loading as $G^H = \sigma_{xy}/\left(2\varepsilon_{xy}\right)$. Table 2 summarizes the effective Young's and shear moduli measured for the structures with different periods. For the RMS, the measured properties converge to the effective material properties predicted using the homogenization method for infinite periodicity. This is not the case for the OMS, where Young's modulus deviates by 2% and shear modulus by 22%. The main reason for this deviation is the difference in effective Poisson's ratio between the RMS with a near-zero Poisson's ratio and OMS with a finite Poisson's ratio. For zero Poisson's ratio, the fixed vertical displacement boundary conditions at left and right edges have no effect on the macroscopic response, whereas the opposite is the case when the Poisson's ratio is non-zero as in the OMS case.

Table 1 Effective material properties for the infinitely periodic materials and material buckling stress for uniaxial compression and pure shear stress

	E^H	ν^H	G^H	κ^H	$\sigma_{xx}^{cri}\left[10^{-3}\right]$	$\sigma_{xy}^{cri}\left[10^{-3}\right]$
RMS	0.1638	0.0592	0.0024	0.0871	2.21	1.86
OMS	0.0952	0.3553	0.0162	0.0738	9.88	6.19

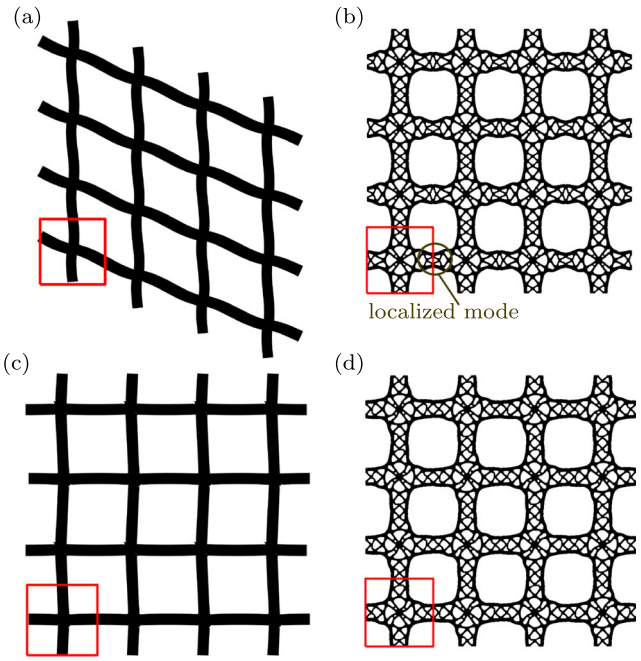

Fig. 2 Critical material buckling modes for infinitely periodic case, for the unixial compression (Top: (**a**) and (**b**)) and pure shear loading (bottom: (**c**) and (**d**))

3.1 Buckling evaluation for uniaxial compression

Under uniaxial compression, Fig. 3 shows the first six linear buckling modes of the structure formed from 4-by-4 periods of the RMS. It is seen that the critical buckling mode is the global shear mode in accordance with the critical material mode shown in Fig. 2. However, due to boundary stiffening effects, the structural critical buckling strength is around 12% higher than that for the infinitely periodic case.

In the PB evaluation, we first consider the imperfection stemming from the first buckling mode in Fig. 3 to investigate the influence of maximum perturbation amplitude on the PB evaluation considering the maximum perturbation amplitude of $\varphi = 0.0001$ denoted by the army-green line and $\varphi = 0.0005$ denoted by the black line in Fig. 4. In both cases, a small stiffening effect is observed, which leads

Table 2 Measured Young's and shear moduli in finite structures

	Infill	$N = 2$	$N = 4$	$N = 6$	$N = 8$	$N = \infty$
E^H	RMS	0.1642	0.1640	0.1640	0.1639	0.1638
	OMS	0.0950	0.0960	0.0963	0.0963	0.0952
G^H	RMS	0.0031	0.0025	0.0024	0.0024	0.0024
	OMS	0.0127	0.0128	0.0128	0.0127	0.0162

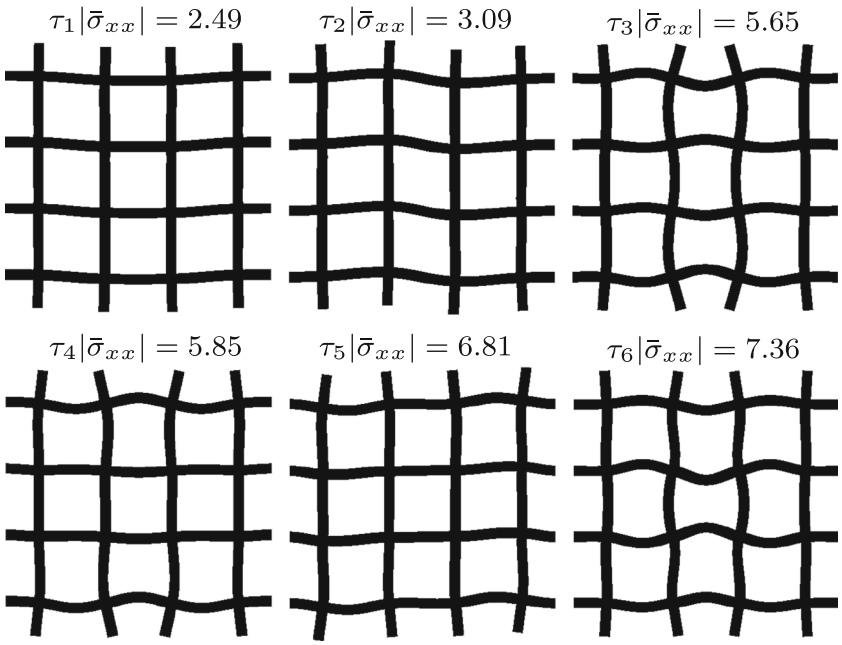

Fig. 3 First six buckling modes obtained from the LB analysis of the structure formed from the RMS with corresponding buckling stress [10^{-3}]. Top row from left to right: the first, second, and third buckling modes; bottom row from left to right: the forth, fifth, and sixth buckling modes

to higher buckling stress in the PB analysis than the LB analysis represented by the blue line. The red circles in the lines highlight the critical buckling stress. The intersection between the strain–stress curve for the perfect structure denoted by the green dash-dot line and the corresponding pre-buckling prediction denoted by the red dash-dot line indicates the buckling stress from the NPB prediction. It is seen that higher perturbation amplitude leads to a smaller buckling stress in the PB evaluation, and that the buckling stress is closer to the NPB prediction as the perturbation amplitude reduces. The final deformation patterns in both cases are same as the first buckling mode in Fig. 3. Considering that the perturbation of $\varphi = 0.0001$ is very small, we fix the max perturbation amplitude to be $\varphi = 0.0005$, hereafter, unless otherwise stated.

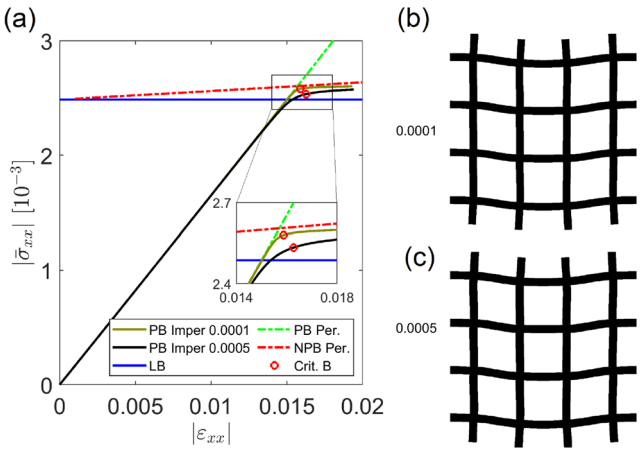

Fig. 4 Influence of imperfection amplitudes in the PB analysis. **a** Evaluation results. Structural deformation pattern for **b** $\Phi = 0.0001$ and **c** $\Phi = 0.0005$

Figure 5 summarizes the PB evaluations for two different geometric imperfections stemming from buckling modes in Fig. 3, i.e., (1) the critical buckling mode; (2) an equal-weighted superposition of the first six modes. The structure with only the first imperfection performs slightly softer than the one with multiple superimposed imperfections under finite deformations. Hence, the first imperfection results in lower critical buckling strength. The deviation of the buckling strength in these two cases is small, however, and final deformation patterns are equal, i.e., the global shear mode (see Fig. 5b, c).

Next, we perform the same analysis for the optimized infill structure to investigate the influence of imperfection

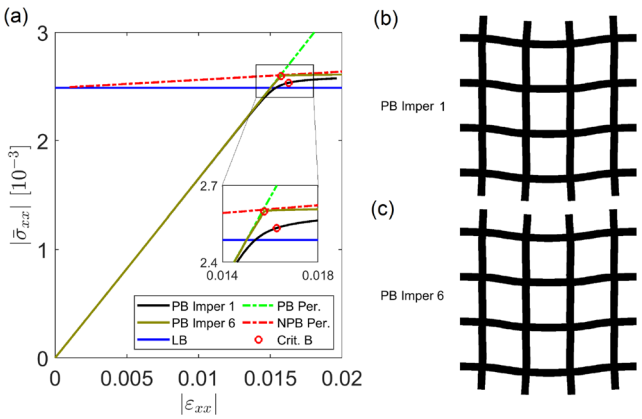

Fig. 5 **a** Stress–strain curves under uniaxial compression for the benchmark problem considering different imperfections. The red symbols indicate the critical buckling stress. **b** Deformation pattern with imperfection stemming from the first buckling mode; **c** deformation pattern with imperfection stemming from the equal-weighted superposition of the first six buckling modes

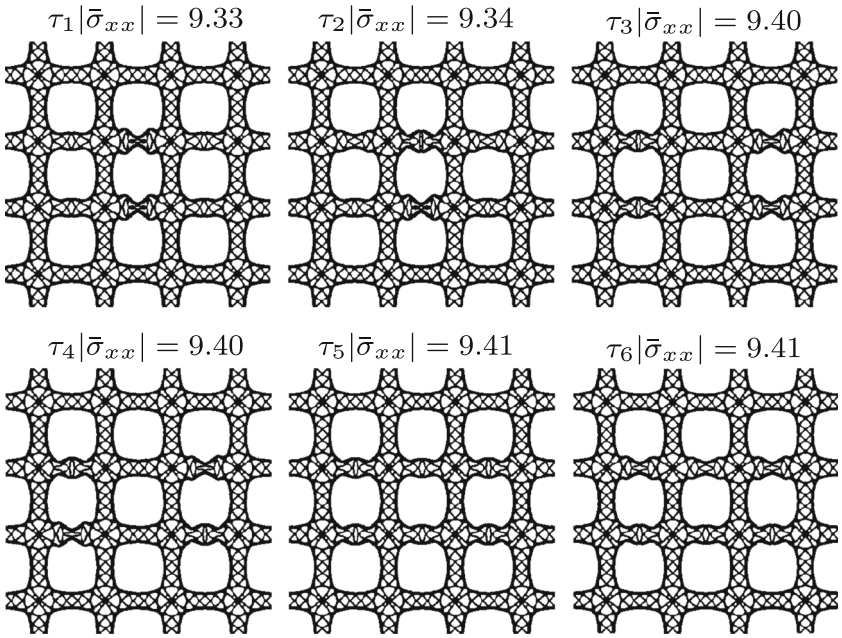

Fig. 6 First six buckling modes from LB analysis of the structure formed from the OMS with corresponding buckling stress [10^{-3}]. Top row: from left to right: the first, second and third buckling mode; bottom row from left to right: the forth, fifth, and sixth buckling modes

patterns on the PB evaluations. In contrast to the RMS structure, the first six buckling modes are all local modes located at interfaces between unit cells with close valued buckling stresses, as seen in Fig. 6. This observation coincides with the material buckling analysis where a cluster of buckling modes exhibits similar buckling stresses. Moreover, the two different geometric imperfections result in two different buckling modes in the PB evaluation, as shown in Fig. 7b, c. Structural softening is observed for both perturbed structures as illustrated by the reduced tangent stiffness in the stress–strain curve. Same as for the previous case, the second geometric imperfection leads to higher buckling stress in the PB evaluations.

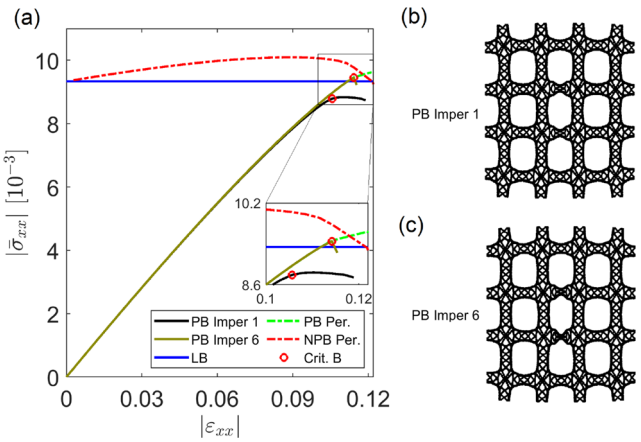

Fig. 7 **a** Stress–strain curves under the uniaxial compression of the structure infilled with the OMS considering different imperfections. The red symbols indicate the critical buckling stress; **b** deformation pattern when imperfection stems from the first buckling mode; **c** deformation pattern when imperfection stems from the equal-weighted superposition of the first six buckling modes

Based on above observations, we focus on numerical investigations considering the geometric imperfection from the first buckling mode in the subsequent cases. Figure 8 summarizes the critical buckling stress for both structures, obtained from the LB, PB, and NPB analyses. It is seen that the OMS structure can undergo much larger deformations than the RMS and that it behaves softer and buckles at a higher stress level. For both structures, the buckling stress predicted from the NPB analysis is higher than the one from the LB analysis due to geometric and material nonlinearities, and geometric imperfections result in lower buckling stress compared to the one predicted from the NPB analysis. However, the difference between these two predictions is smaller for the RMS compared to the OMS. This observation further demonstrates that the OMS is more vulnerable to imperfections.

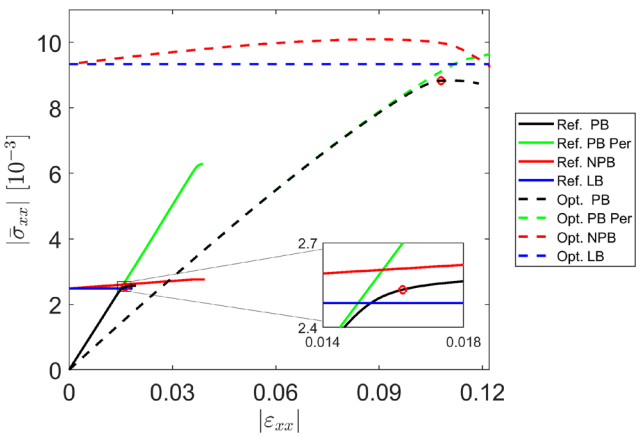

Fig. 8 Overall evaluations of the buckling stresses of structures formed from the RMS and OMS using the LB, PB, and NPB analyses

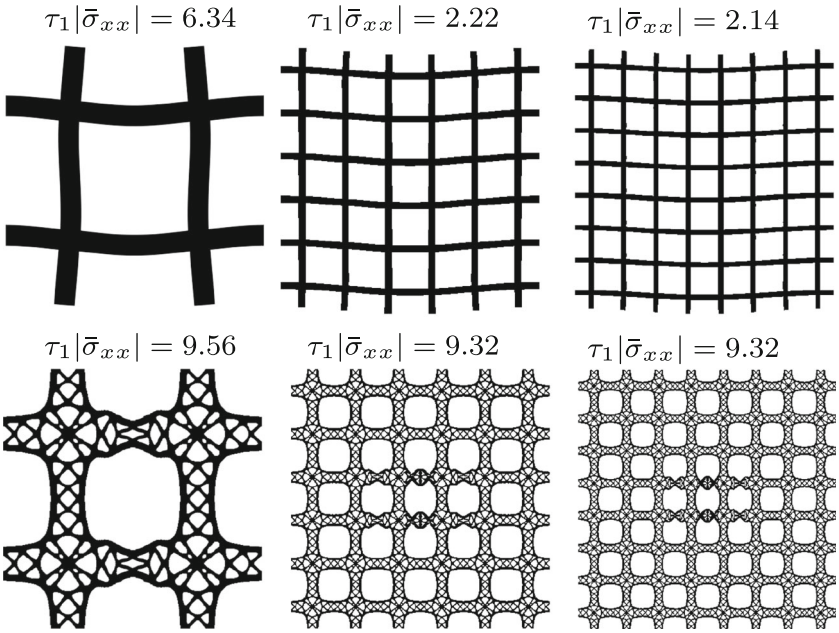

Fig. 9 First buckling modes of the structures with different periods with critical buckling stress [10^{-3}]. Top: RMS; bottom: OMS

Figure 9 shows the critical LB modes for structures with different numbers of infill periods and the corresponding buckling stresses. The critical buckling mode of the RMS structures is a global shear mode. The corresponding critical buckling stress decreases as the unit cell number increases and boundary stiffening effects diminish. However, for the OMS, the critical buckling modes are local modes dependent on the number of periods. The buckling modes are located at the two center unit cells in the vertical direction, but buckling modes span different unit cells in the lateral directions. The critical buckling stress stays almost constant as the unit cell period reaches 4, and much smaller deviations are observed in the LB predicted buckling stress, compared to the RMS.

Table 3 summarizes the results for the structures with different periods of unit cells. It is seen that predicted buckling stresses using LB, PB, and NPB analyses decrease as the unit cell period increases for the RMS. A dramatic decrease in the buckling stress is observed from 2-by-2 unit cells to more periods because the boundary stiffening effects are smaller as the periods increase. In general, slightly higher buckling stress is obtained from the PB analysis than the one from the LB analysis due to stress stiffening effects. Moreover, the NPB analysis predicts the highest critical buckling stress due to geometric and material nonlinearities and lack of imperfections.

The overall assessment shows that the OMS structures exhibit much larger buckling stress than the RMS structures, which is in line with the linear material prediction. Hence, it may be concluded that optimization based on linear buckling analysis in this case has not overestimated the actual nonlinear buckling response as otherwise often feared.

Table 3 Buckling strength of the structures with different periods of unit cells under the unixial compression evaluated using different numerical approaches $[10^{-3}]$

Unit cells	RMS			OMS		
	LB	PB	NPB	LB	PB	NPB
$N = 2$	6.34	6.86	7.10	9.56	9.48	9.56
$N = 4$	2.49	2.53	2.60	9.33	8.79	9.77
$N = 6$	2.22	2.24	2.31	9.32	9.21	9.76
$N = 8$	2.14	2.15	2.21	9.32	8.73	9.65
$N = \infty$	2.21	–	–	9.88	–	–

3.2 Buckling evaluation for shear loading

Next, we perform a similar analysis for shear loading keeping in mind that the OMS structure was not specifically optimized for shear loading.

Figure 10 shows the critical buckling modes for the structures formed from 4-by-4 RMSs and OMSs. The critical

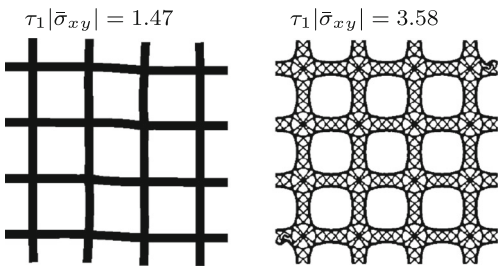

Fig. 10 Critical buckling modes under shear loading from LB analysis [10^{-3}]. Left: RMS. Right: OMS

buckling mode is a global shear deformation pattern for the RMS structure. The corresponding structural buckling stress is smaller than the material buckling stress listed in Table 1. Only a local boundary deformation pattern is observed in the OMS structure, where apparently, the critical buckling mode is induced by boundary effects, which cause stress concentrations at the lower left corner. Hence, the corresponding structural buckling stress is much smaller than the material buckling stress. The OMS structure exhibits 2.4 times the buckling strength of the RMS structure in LB analysis. Compared to the material evaluation in Table 1, the buckling strength enhancement in the OMS structure degrades due to the boundary effects of the finite structures.

Figure 11a summarizes the overall evaluations from the LB, NPB, and PB analyses. The geometric imperfections used are the same as in the uniaxial compression case. Hence, in the PB analysis, the considered imperfections are fixed to be the first buckling modes shown in Fig. 10 with the maximum perturbation amplitude $\varphi = 0.0005$.

Under shear loading, the OMS structure represented by dashed lines is stiffer than the RMS structure represented by solid lines. Deformation stiffening is observed in both structures due to the geometrically nonlinear stretching under shear loading. For the structure with the OMS, the PB analysis stops just below the NPB predicted buckling stress. For the structure with the RMS, no NPB prediction is available

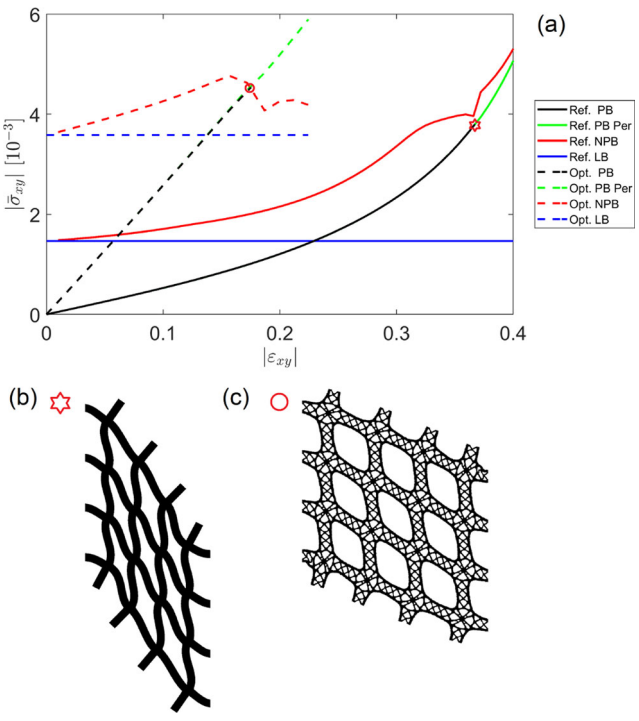

Fig. 11 **a** Overall evaluations of the buckling stress for the structures with the RMS and OMS using the LB, NPB and PB analyses under shear loading. **b** Deformation pattern of the structure with the RMS. **c** Deformation pattern of the structure with the OMS

because no intersection between the strain–stress curve and pre-buckling prediction is observed. In the PB analysis, the arc-length method is unable to find a converged solution using the employed computational strategy mentioned at the end of Section 2 after a certain number of increment steps. Hence, the last converged result in the PB analysis is used as the buckling prediction from the PB analysis. The corresponding deformation patterns in Fig. 11b, c demonstrate that both structures have buckled. Compared to the RMS structure, the OMS structure buckles at a much smaller shear strain. The corresponding buckling strength enhancement of the OMS is much smaller, compared to the results from the LB analysis and material prediction in Table 1.

Table 4 summarizes the critical buckling stresses based on the LB and PB analyses. The LB predictions show that the buckling enhancement of the OMS structure degrades under shear loading. In the PB analysis, the last converged stresses are used to represent the critical buckling stress. It is seen that all the structures exhibit much higher buckling stresses in the PB analysis than the ones from the LB analysis, due to the geometrically nonlinear stretching under shear loading. Moreover, the critical buckling stress decreases as the period number increases. In contrast, the RMS structures show much higher buckling stress in the PB analysis than the material prediction. However, the OMS structures exhibit much lower buckling stress than the material prediction due to the boundary-induced buckling modes in the finite structures. Clearly, the predicted buckling strength from the material analysis has diminished due to boundary effects, material nonlinearities, and geometrical nonlinearities in particular.

4 Discussion

Our study confirms that finite structures infilled with OMSs optimized for infinite periodicity, infinitesimal strain assumption, and linear buckling analysis in Thomsen et al. (2018) can effectively enhance infill buckling strength with

Table 4 Buckling strength of the structures under shear loading with different periods of unit cells evaluated using different numerical approaches $[10^{-3}]$

Unit cells	RMS		OMS	
	LB	PB	LB	PB
$N = 2$	1.57	3.76	3.52	4.67
$N = 4$	1.47	3.88	3.58	4.46
$N = 6$	1.59	3.54	3.17	3.54
$N = 8$	1.63	2.95	2.86	3.19
$N = \infty$	1.86	–	6.19	–

small decrease in stiffness, as illustrated by the uniaxial compression case. Hence, even if LB analysis does not take geometric and material nonlinear effects into account, it can effectively be used in a topology optimization process to produce efficient infill structures. However, our study also shows that LB predictions of shear buckling response, for which the OMS was not optimized, is highly inaccurate and cannot be trusted. This is not an unexpected conclusion since a softer structure in shear yields higher deformations that in turn cannot be predicted accurately by the linear model. Despite this conclusion, we note that the finite structures based on OMS still perform better in shear than the corresponding RMS-based structures.

We remark that an isotropic buckling optimized hierarchical triangular microstructure was also designed in Thomsen et al. (2018). It may in future studies be interesting to investigate if linear predictions of this microstructure subjected to shear loads are more accurate than the predictions for the orthotopic structure considered here. When only considering stiffness criteria, orthotropic infill is much more efficient than isotropic counterparts (c.f. Groen et al. (2019)); however, more work still needs to be done to fully understand the connection between microscopic and macroscopic buckling criteria.

Another direction for future research is the use of finite deformations directly in the microstructure optimization formulation, possibly according to theory presented in Geymonat et al. (1993) and Triantafyllidis and Schnaidt (1993). Deeper investigations of geometrically nonlinear effects in infinitely periodic structures are performed in our parallel work (Bluhm et al. 2020).

5 Conclusion

This study has systematically investigated the performances of simple and optimized periodic infill structures (OMS) in terms of finite scale stiffness and buckling. The buckling is evaluated by linear buckling, nonlinear pre-buckling, and post-buckling analyses. Under uniaxial compression, the simple infill structures perform relatively linearly and buckle at small deformations. This means that all three evaluation methods provide close predictions on the critical buckling stress, and hence that linear buckling analysis was sufficient as a base for the optimization in Thomsen et al. (2018). In contrast, the buckling strength enhancement of the OMS predicted using linear material buckling analysis diminishes in the finite structure evaluation under shear loading, due to boundary-induced buckling modes and geometric and material nonlinearities. Nevertheless, the overall evaluations indicate that buckling enhancement is significant when aligning the OMS along the principle stress direction compared to their simple RMS counterparts at little decrease in stiffness, supporting the conclusions in Thomsen et al. (2018).

Acknowledgments The authors acknowledge the support of the Villum Fonden through the Villum Investigator Project InnoTop. The authors would like to thank Konstantinos Poulios, Gore Lukas Bluhm, Federico Ferrari in the Department of Mechanical Engineering at Technical University of Denmark for valuable discussions

Compliance with ethical standards

Conflict of interest The authors declare that they have no conflict of interest.

Replication of results All simulations are performed using an in-house MATLAB implementation. The detailed formulations, hyperelastic material law, corresponding references, and parameters used in the PB analysis are listed in the paper to allow replication of results. The considered microstructures can be obtained on reasonable request.

References

Allaire G, Geoffroy-Donders P, Pantz O (2019) Topology optimization of modulated and oriented periodic microstructures by the homogenization method. Comput Math Appl 78(7):2197–2229

Andreassen E, Lazarov B, Sigmund O (2014) Design of manufacturable 3D extremal elastic microstructure. Mech Mater 69(1):1–10

Bendsøe MP, Sigmund O (2003) Topology optimization: theory, methods and applications. Springer, Berlin

Bluhm GL, Sigmund O, Wang F, Poulios K (2020) Nonlinear compressive stability of hyperelastic 2D lattices at finite volume fractions, vol 137

Christiansen RE, Wang F, Sigmund O (2019) Topological insulators by topology optimization. Phys Rev Lett 122(23):234502

Clausen A, Aage N, Sigmund O (2016) Exploiting additive manufacturing infill in topology optimization for improved buckling load. Engineering 2(2):250–257

Clausen A, Wang F, Jensen JS, Sigmund O, Lewis JA (2015) Topology optimized architectures with programmable Poisson's ratio over large deformations. Adv Mater 27(37):5523–5527

Geymonat G, Müller S, Triantafyllidis N (1993) Homogenization of nonlinearly elastic materials, microscopic bifurcation and macroscopic loss of rank-one convexity. Arch Ration Mech Anal 122(3):231–290

Groen JP, Sigmund O (2018) Homogenization-based topology optimization for high-resolution manufacturable microstructures. Int J Numer Methods Eng 113(8):1148–1163

Groen JP, Wu J, Sigmund O (2019) Homogenization-based stiffness optimization and projection of 2D coated structures with orthotropic infill. Comput Methods Appl Mech Eng 349:722–742

Guedes J, Kikuchi N (1990) Preprocessing and postprocessing for materials based on the homogenization method with adaptive finite element methods. Comput Methods Appl Mech Eng 83(2):143–198

Guest JK, Prévost JH (2006) Optimizing multifunctional materials: design of microstructures for maximized stiffness and fluid permeability. Int J Solids Struct 43(22-23):7028–7047

Haghpanah B, Papadopoulos J, Mousanezhad D, Nayeb-Hashemi H, Vaziri A (2014) Buckling of regular, chiral and hierarchical honeycombs under a general macroscopic stress state. Proc R Soc A Math Phys Eng Sci 470(2167):20130856

Huang X, Radman A, Xie YM (2011) Topological design of microstructures of cellular materials for maximum bulk or shear modulus. Comput Mater Sci 50(6):1861–1870

Krenk S (2009) Non-linear modeling and analysis of solids and structures. Cambridge University Press, Cambridge

Larsen UD, Sigmund O, Bouwstra S (1997) Design and fabrication of compliant micromechanisms and structures with negative Poisson's ratio. J Microelectromech Syst 6(2):99–106

Meza L, Zelhofer AJ, Clarke N, Mateos AJ, Kochmann D, Greer J (2015) Resilient 3D hierarchical architected metamaterials. Proc Natl Acad Sci 112(37):11502–11507

Meza LR, Phlipot GP, Portela CM, Maggi A, Montemayor LC, Comella A, Kochmann DM, Greer JR (2017) Reexamining the mechanical property space of three-dimensional lattice architectures. Acta Mater 140:424–432

Neves MM, Sigmund O, Bendsøe M (2002) Topology optimization of periodic microstructures with a penalization of highly localized buckling modes. Int J Numer Methods Eng 54(6):809–834

Neves MM, Sigmund O, Bendsoe MP (2002) Topology optimization of periodic microstructures with a buckling criteria. Vienna University of Technology

Rammerstorfer FG, Pahr DH, Daxner T, Vonach WK (2006) Buckling in thin walled micro and meso structures of lightweight materials and material compounds. Comput Mech 37(6):470–478

Sigmund O (1994) Materials with prescribed constitutive parameters: an inverse homogenization problem. Int J Solids Struct 31(17):2313–2329

Sigmund O (1995) Tailoring materials with prescribed elastic properties. Mech Mater 20(4):351–368

Sigmund O, Torquato S (1997) Design of materials with extreme thermal expansion using a three-phase topology optimization method. J Mech Phys Solids 45(6):1037–1067

Takezawa A, Kobashi M (2017) Design methodology for porous composites with tunable thermal expansion produced by multi-material topology optimization and additive manufacturing. Compos Part B: Eng 131:21–29

Thomsen CR, Wang F, Sigmund O (2018) Buckling strength topology optimization of 2D periodic materials based on linearized bifurcation analysis. Comput Methods Appl Mech Eng 339:115–136

Triantafyllidis N, Schnaidt WC (1993) Comparison of microscopic and macroscopic instabilities in a class of two-dimensional periodic composites. J Mech Phys Solids 41(9):1533–1565

Triantafyllidis N, Schraad MW (1998) Onset of failure in aluminum honeycombs under general in-plane loading. J Mech Phys Solids 46(6):1089–1124

Vogiatzis P, Chen S, Wang X, Li T, Wang L (2017) Topology optimization of multi-material negative Poisson's ratio metamaterials using a reconciled level set method. Comput Aided Des 83:15–32

Wang F (2018) Systematic design of 3D auxetic lattice materials with programmable Poisson's ratio for finite strains. J Mech Phys Solids 114:303–318

Wang X, Xu S, Zhou S, Xu W, Leary M, Choong P, Qian M, Brandt M, Xie YM (2016) Topological design and additive manufacturing of porous metals for bone scaffolds and orthopaedic implants: a review. Biomaterials 83:127–141

Wriggers P (2008) Nonlinear finite element methods. Springer, Berlin

Wu J, Aage N, Westermann R, Sigmund O (2017) Infill optimization for additive manufacturing—approaching bone-like porous structures. IEEE Trans Vis Comput Graph 24(2):1127–1140

Zheng X, Smith W, Jackson J, Moran B, Cui H, Chen D, Ye J, Fang N, Rodriguez N, Weisgraber T (2016) Multiscale metallic metamaterials. Nat Mater 15(10):1100

Zienkiewicz OC, Taylor RL (2005) The finite element method for solid and structural mechanics. Elsevier Butterworth-Heinemann, Amsterdam